Original Research

Structure-Property-Performance Correlation of Sol-Gel Derived ZnO Thin Films for High-Efficiency Solar Cell Applications: A Combined Experimental and Computational Study

Pramod Mandal[1], Anand Pandey[2], Sudesna Roy[3,*]

[1] Department of Graphic Arts and Photophysics, Faculty of Chemical Technology, University of Pardubice, Pardubice-532 10, Czech Republic

[2] Department of Physics, Chemistry and Biology (IFM), Linköping University-581 83, Sweden

[3] School of Mechanical Engineering, KIIT Deemed to be University, Bhubaneswar-751024, India

* Correspondence: sudesna.roy@gmail.com

Received: February 10, 2025; Accepted: April 13, 2026

Abstract: In this manuscript, we have comprehensively investigated the structural, optical, photoluminescence (PL), and Raman spectra of sol-gel-synthesized ZnO thin films using a combination of experimental and theoretical approaches. The deposited ZnO thin film was further characterized using scanning electron microscopy (SEM) with elemental dispersive spectroscopy (EDS), atomic force microscopy (AFM), X-ray diffraction (XRD), UV-visible spectroscopy, photoluminescence (PL), and Raman spectroscopy. XRD and UV-Vis. Results suggested that the as-synthesized ZnO film is a uniform thin film with an average surface roughness of 5.5 ± 0.5, and that it has a wurtzite structure, as confirmed by XRD analysis. Moreover, the optical bandgap (E_g) was determined to be 3.39 eV. In contrast, EDS analysis confirms the presence of Zn and O atoms in the thin film. PL and Raman measurements reveal thin-film defect levels, possibly due to Zn interstitials, oxygen vacancies, and nonradiative recombination. A first-principles DFT study has been conducted to validate the experimental finding. The electronic band structure (3.37 eV) and absorption edge (393 nm) obtained from the DFT calculation were well-matched with the experimental findings. Also, theoretical Raman spectra confirm the wurtzite structure of ZnO and support our experimental Raman data. The synergy between experimental studies and theoretical insights into the material's properties is necessary to highlight its potential for future solar cell applications.

Keywords: ZnO (Zinc oxide); photoluminescence(PL); raman spectra; optoelectronics; DFT (density functional theory).

1. Introduction

Recently, Zinc oxide (ZnO), with the most stable hexagonal wurtzite structure, has emerged as one of the potential metal-oxide semiconductor materials used for a multitude of applications, including solar cells, gas sensors, photodetectors, photo-catalysis, laser systems, optoelectronic devices, and transparent conducting electrodes[1][2][3]. It possesses a direct bandgap semiconductor of n-type conductivity with a high exciton binding energy (60 meV)[4], a wide energy band-gap (E_g) of 3.37-3.40 eV[5][6][7], high electron mobility (up to 155 $cm^2 . V^{-1} . S^{-1}$)[8], and excellent transparency in the visible region. It is also chemically and thermally stable in harsh environments [9][3]. Various methods have been utilized to fabricate ZnO thin films, such as spray pyrolysis[1], radio frequency (RF) magnetron sputtering[10], Pulsed laser deposition (PLD)[11][12], molecular

beam epitaxy (MBE)[13], Chemical vapour deposition (CVD)[14], Chemical bath deposition[15], spin coating[16][17], and dip coating [18]. In the thin-film fabrication process, selecting a cost-effective method, substrate type, and thin-film composition is significant. RF sputtering, PLD, MBE, and CVD methods can produce thin films in a controlled manner with accurate deposition rates. However, these methods are more expensive and less readily available than sol-gel and spray pyrolysis methods. The choice of thin-film deposition method depends on several factors, including material requirements, composition control, thickness, and cost. This manuscript used the sol-gel method to deposit the ZnO thin film. It is one of the most cost-effective and versatile methods for depositing ZnO thin films, offering lower cost, well-controlled thickness, and excellent thin-film quality [18]. However, it also has demerits, *i.e*., limitations in thickness and deposition rate of the thin film. Sol-gel is often used in spin or dip-coating processes due to its relatively low cost and simplicity.

Numerous studies on the deposition of ZnO thin films using the sol-gel method have been performed recently. Selected works from the literature are reviewed in this context, such as those by Moussa *et al*.[19] used the sol-gel spin-coating process to deposit a thin ZnO film for CMOS devices. They concluded a uniform ZnO thin film with no defects using the sol-gel method. Optical analysis indicated an average optical transparency of 98% and an energy bandgap (E_g) of 3.42 eV for the thin film. These properties suggested potential for CMOS application. Similarly, Chavez *et al*. [20] also used the same technique to deposit a ZnO thin film and reported the production of a high-quality film with an average grain size of 20-60 nm, grown over the entire substrate. And Federenko *et al*.[21] had fabricated a sol-gel ZnO thin film for sensor applications and concluded that it could be used for both sensor and photoelectronic applications. Thus, the above report indicates that sol-gel is an effective technique for producing ZnO thin films for various applications. A few studies also reported theoretical research on ZnO material properties using DFT (density functional theory). Wang *et al*.[22] explored the electronic structure and optical characteristics of Tb(terbium) doped ZnO using a GGA+U method and found that the O 2p state causes band-to-band transitions in ZnO in the topmost valence band and the Zn 4s state in the bottom conduction band. Also, Yakoob *et al.* [23] investigated an LDA+U study of ZnO and concluded that structural properties, optical, and elastic properties obtained from the study were consistent with experimental data. The Hubbard U parameter was reported to improve the elastic properties. And Mansy *et al*.[24] explored the structural, optical, and electrical characteristics of ZnO nanoparticles using both computational and experimental methods, and concluded that the geometrical and optical characteristics agreed well with both. Both experiments demonstrate strong absorption in the visible and ultraviolet (UV) regions.

After reviewing the existing literature on experimental and DFT-based outcomes for ZnO, we identified that no exhaustive investigation of its structural, optical, photoluminescence (PL), and Raman properties has yet been reported. While ZnO thin films prepared by the sol-gel method have been widely studied, the novelty of this work lies in the combined experimental investigation and validation through first-principles computational analysis. This integrated approach provides a deeper correlation between the experimentally observed properties and the theoretically predicted electronic structure.

2. Materials and methods

2.1. Experimental details

0.35 M zinc acetate dihydrate precursor solution was produced by dissolving zinc acetate dihydrate into methoxy ethanol and ethanolamine, as per our published reports [25]. This solution was stirred at 60 °C for 1 hr, then aged at room temperature for 48 hrs. The ZnO thin films were fabricated by spin-coating the

precursor solution onto cleaned, pre-patterned fluorine-doped tin oxide (FTO) glass substrates at 3000 rpm for 30 sec. The ZnO films were then annealed at 200°C for 30 minutes on a hot plate 2 for onset of crystallization. This technique was repeated five times to ensure dense and uniform film coverage. The estimated average film thickness of the sample was 300 nm using a surface profilometer, Veeco (Dektak 150). Figure 1 illustrates the schematic diagram for the synthesis of ZnO thin films[26].

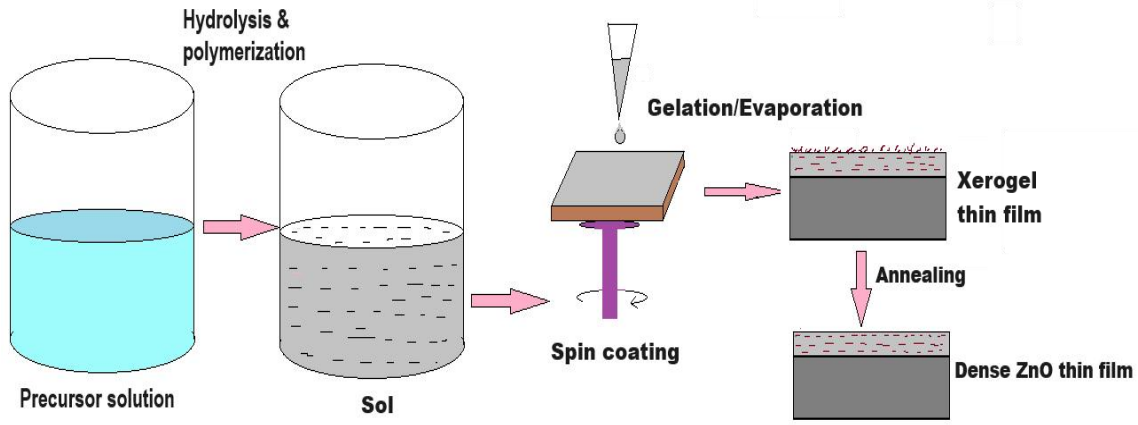

Figure 1. Process flow diagram of the synthesis of ZnO thin film.

2.2. Characterization method

Scanning electron microscopy (SEM) (Tungsten-Electron Microscope (W-SEM)) equipped with EDX was utilized for surface morphology analysis of ZnO thin films. Furthermore, an atomic force microscope (AFM) (Asylum MFP-3D) was used for analysis of the quality of the thin film, an XRD diffractometer using CuK_{α} radiation (λ=0.15405 nm) for the structural analysis, and UV-Vis. Spectrophotometer (Unicam 5625) for the optical properties, Photoluminescence (PL), and Raman analysis were characterized in steady-state at room temperature using a PL spectrophotometer (LAbRAM HR, Horiba) with the laser excitation at 325 nm and Raman analysis using laser excitation of 532 nm.

2.3. Computational details

A Computional study was performed using density functional theory (DFT) to support the experimental finding. The CASTEP (Cambridge Serial Total Energy Package) was used for the entire study[27][28], which is based on the Schrodinger equation [29]. The generalized gradient approximation (GGA) with the Perdew-Burke-Ernzerhof (PBE) functional and the Broyden-Fletcher-Goldfarb-Shanno (BFGS) optimization method were employed throughout the experiment. Parameters such as energy cut-off (380 eV), SCF tolerance (5.0×10^{-7} eV.Å), and Monkhorst-Pack (K) points of (5 × 5 × 4) in the Brillouin zone path were selected for the simulation study. The study also included the maximum displacement (5×10^{-4} Å), maximum force (0.01 eV/Å), and maximum stress (0.02 GPa) as additional parameters. All the simulations had occurred in the Brillouin zone path, i.e., G (000)-A (0,0,0.5)-H (-0.33,0.667,0.5)-K (-0.33,0.667,0)-G (000)-M ((0,0.5,0)-L (0,0.5,0.5). Further, the electronic states for Zn atoms $3d^{10}$ $4s^2$, and O atoms $2s^2$ $2p^4$, were considered the valence state for the Pseudo-atomic calculation. A local density approximation(LDA)+U study was considered in this study to obtain the accurate band structure of ZnO [24]. As is well known, the LDA (GGA) study is based on ground-state theory. It underestimates the exchange-correlation potential between excited electronic states, giving a much lower energy band gap than the experimental energy band gap [30]. Finally, for the analysis of Raman spectra from the simulation, a Pseudopotential norm-converging method was used, and all parameters were kept the same.

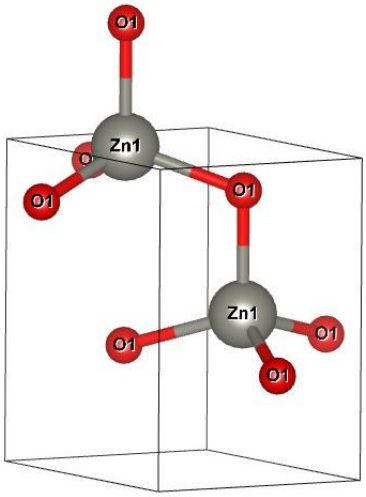

Figure 2. Optimized Unit structure of ZnO exported from Vesta software.

3. Results

3.1 Surface morphology and compositional analysis (EDX)

Figure 3 shows a typical SEM micrograph of ZnO thin films; topographical analysis indicates that the thin film was homogeneous and defect-free. The granules in the thin film were evenly distributed across the substrate. Furthermore, AFM analysis was performed to evaluate the thin film quality, as shown in Figure 4. The AFM investigation revealed an average root-mean-square (RMS) value of 5.5 ± 0.5 nm, indicating a smoother surface finish for the thin film.

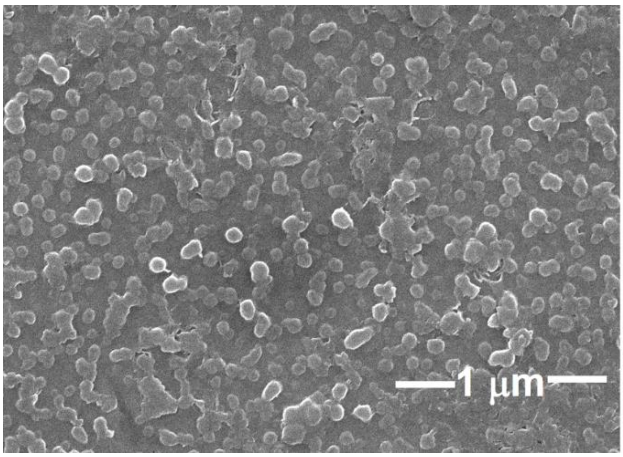

Figure 3. SEM micrograph of the grown ZnO thin film.

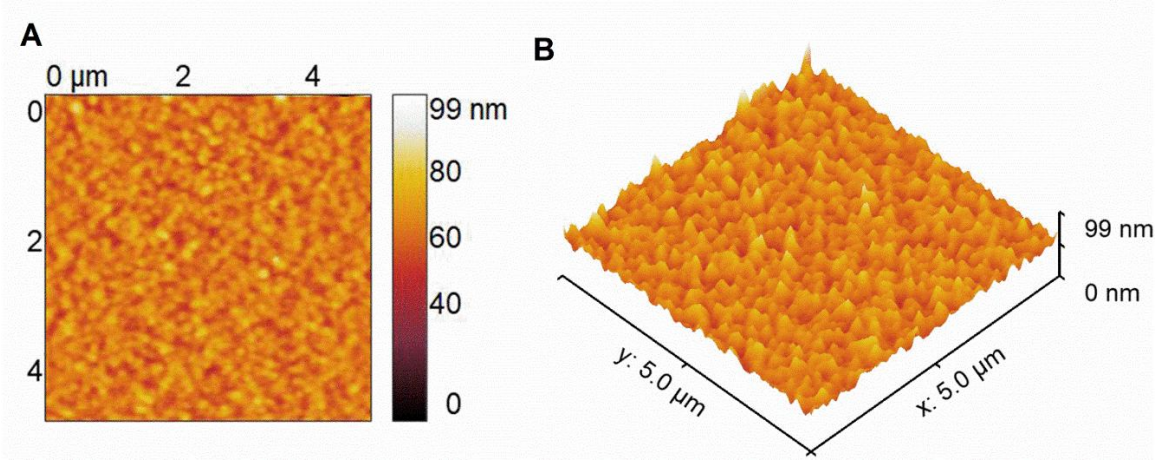

Figure 4. Top view AFM (A) 2D surface profile and (B) 3D micrograph of ZnO thin film.

Furthermore, compositional analysis of the ZnO thin film was performed using EDX to determine the types of neighbouring elements present, as shown in Figure 5. The EDX spectra show the elements contained in the thin films as weight (%) [Zinc- 25.7, oxygen- 17.2, Tin- 46.1, gold- 3.6, sodium- 2.5, palladium- 2.1, silicon- 1.9, Chlorine- 0.4]. The dominant presence of Zn and O confirms the successful deposition of ZnO thin film. The remaining elements most likely originate from the substrate, the deposition environment, or the sample preparation process.

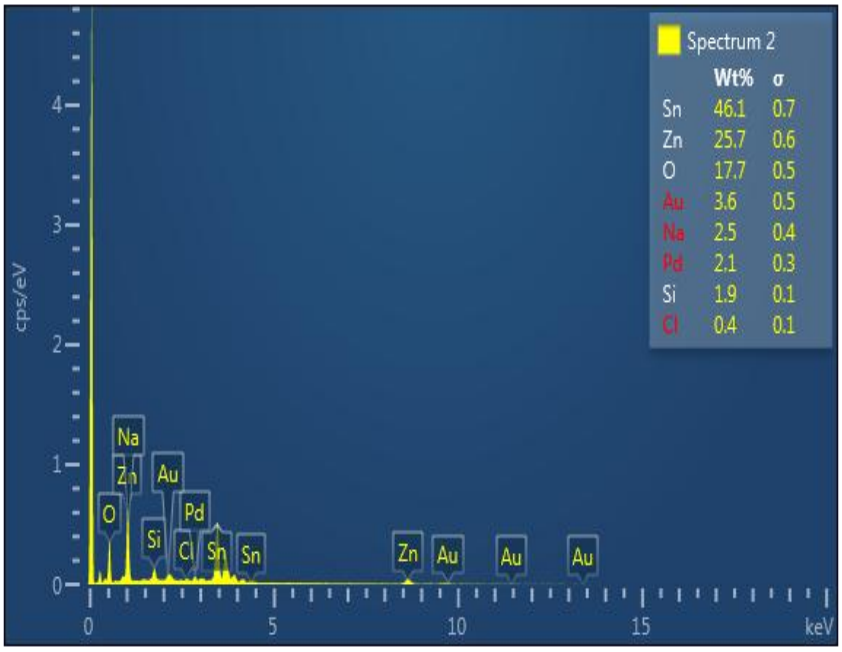

Figure 5. EDX spectra of the ZnO thin film.

3.2. Structural and phase properties

The structural properties and phase identification of ZnO thin film were investigated using XRD, as shown in Figure 6(b). From the analysis, the obtained thin film was polycrystalline ZnO. Where XRD peaks (100), (002), (101), and (102) planes corresponded to the 31.7°, 34.3°, 36.2°, and 47.5°, respectively, similar results were also obtained in the published report [31]. The sharp, high-intensity peaks in the XRD pattern of the thin film indicate good crystallinity all over the substrate. Furthermore, the lattice parameter was extracted as: a (Å) =b (Å)=3.25, c(Å) =5.20, and cell volume = 47.62 ($Å^3$) using the JCPDS File no.00-36-1451. Additionally, the Scherrer formula (equation 1) was used to determine the crystallite size (d) of the ZnO thin

film.

Scherrer formula, $$d = \frac{k\gamma}{\beta cos\theta} \quad (1)$$

Where k is the Scherer constant (considered to be 0.9), γ is the wavelength of the x-ray source (0.154 nm), β is the full width half maxima (in radians), and is the peak position (in degrees). The crystallite size was determined to be 16.21 ± 0.5 nm.

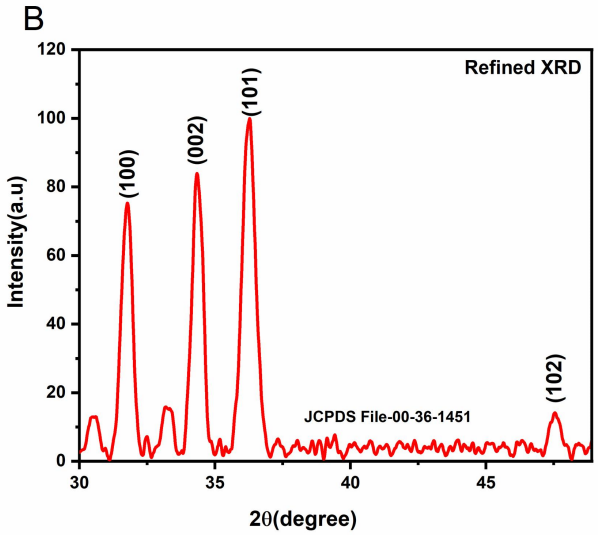

Figure 6. XRD pattern of ZnO thin film.

3.3 Optical properties

3.3.1 UV-visible spectroscopy

The UV-Vis Spectrophotometer was used to study the optical properties, *i.e.*, the absorbance vs wavelength curve and the energy bandgap (E_g) of the ZnO thin film, using Tauc's plot (Figure 7). Figure 7(A) shows the absorbance vs wavelength curve of the ZnO thin film, the absorption edge observed to be at 393 nm wavelength, which is consistent with the result as reported[32][31] For ZnO. Furthermore, the optical band gap of the thin film was calculated using the following equations (2) and (3);

$$(\alpha h\nu)^n = C(h\nu - E_g) \quad (2)$$

$$\alpha = 2.303\frac{\mathrm{A}}{t} \quad (3)$$

Where E_g is the energy bandgap, α is the absorption coefficient, hν is the Photon energy of the ZnO thin film, A is the absorbance, t is the measured thickness of the ZnO thin film, C is a constant, and n is the class of the transition process (where n=2 for direct band gap and 1/2 for indirect band gap). The E_g of the ZnO thin film obtained using the Tauc's plot was 3.39 eV, as depicted in Figure 7(B) inset, consistent with the published report for the ZnO thin film [33][34].

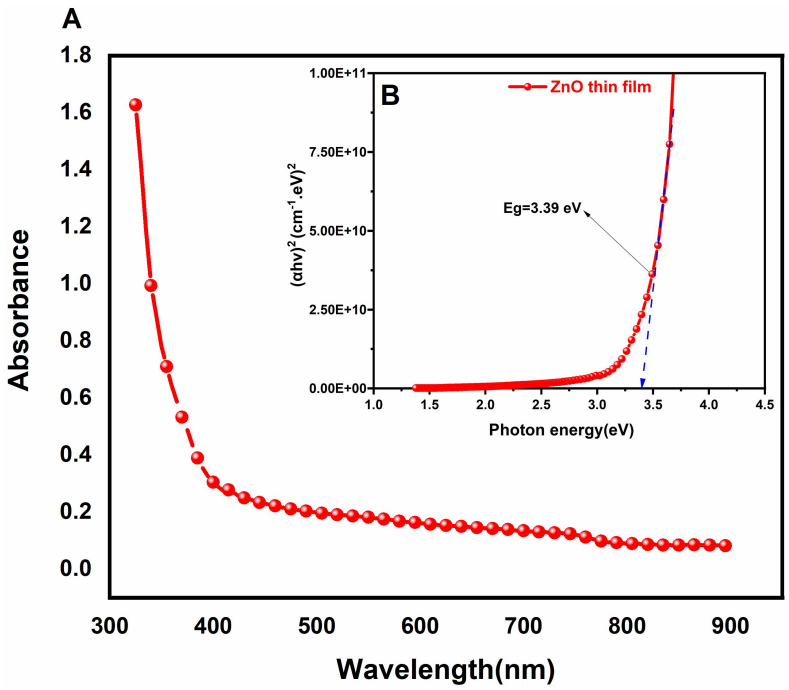

Figure 7. Variation of absorbance against the wavelength, with the Tauc plot (inset).

3.3.2 *Photoluminescence (PL) properties*

Figure 8 depicts the photoluminescence (PL) spectra of the ZnO film. The PL spectra show peaks at 375 nm, 502 nm, 567 nm, 592 nm, and 745 nm. The peak corresponding to 375 nm is attributed to a direct band-to-band transition or a narrow band emission peak (NBE) [25][35]. Other peaks at 502 nm, 567 nm, 592 nm, and 745 nm were due to non-radiative recombination or deep-level emission (DLE) defects. Among various peaks observed in DLE defects, 502 nm, 567 nm, and 592 nm are green emission bands, yellow-green emission bands, and yellow emission bands, respectively [36]. The green emission band originates from the oxygen vacancies, whereas the yellow-green emission emerges from the oxygen interstitials. The yellow emission band arises from doubly ionised oxygen vacancies. The PL peak appears at 745 nm and arises from a near-infrared (NIR) transition. [36][37]. The NIR emission observed at 745 nm can be attributed to radiative recombination between deeply trapped holes and shallowly trapped electrons at oxygen interstitials. Alternatively, it may result from donor-acceptor transitions between oxygen vacancies and zinc interstitial defects. The intensity of this emission likely depends on the concentration of these defect states. Thus, PL analysis of ZnO films indicates that they contain multiple nonradiative defect levels within the energy band gap. These defects intrinsically appear in the ZnO films and can be tuned with doping, annealing, and/or surface passivation [38][39].

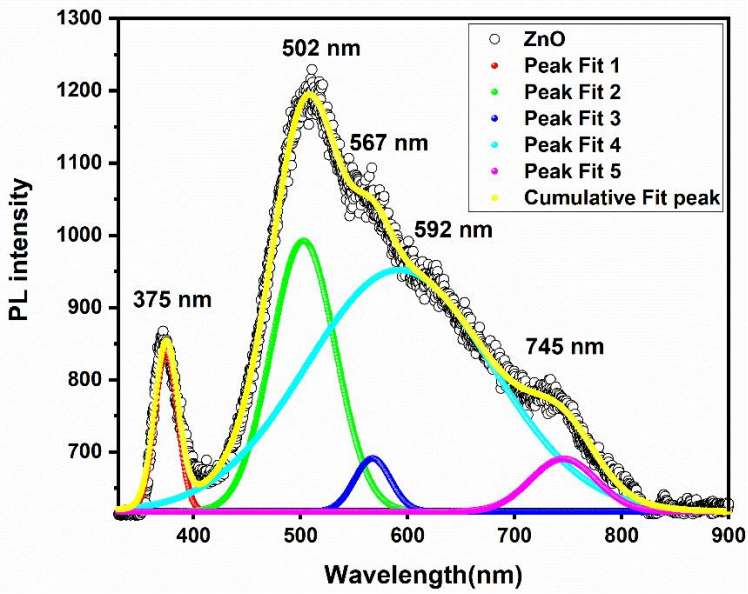

Figure 8. Deconvoluted Photoluminescence spectra of sol-gel fabricated ZnO thin film.

3.4. Raman analysis

Figure 9 shows the Raman spectra of ZnO thin film. The Raman spectra of ZnO films display Raman signals corresponding to 187 cm^{-1}, 419 cm^{-1}, 573 cm^{-1}, 777 cm^{-1}, 971 cm^{-1}, and 1091 cm^{-1}. The band appears at 187 cm^{-1}, 971 cm^{-1}, and 1091 cm^{-1} due to the second-order features involving LO combinations and overtones [40][41][42]. Whereas the bands appearing at 419 cm^{-1} and 573 cm^{-1} are identified as E2 (high) and A1 (LO) modes of ZnO wurtzite structure [41]. The Raman band at 187 cm^{-1} is identified as the 2E2 (low) mode, which arises from zinc interstitial defects. [43]. The asymmetric peak at 419 cm^{-1} and 573 cm^{-1} is due to the overlap of two modes, A1 (LO) and E1(LO) [44]. These modes correspond to the main Raman signal from oxygen vacancies in ZnO. Further, grain size and crystallite size play a crucial role in determining the optical and vibrational properties of semiconductors. Larger grains typically exhibit stronger and sharper PL due to fewer grain boundaries, which act as non-radiative recombination centres, while smaller grains often show reduced PL intensity and broader emission due to increased defect sites [45]. In Raman spectroscopy, larger grains lead to sharper, more intense peaks with minimal phonon confinement, whereas smaller grains cause peak broadening, shifts, and enhanced defect-related modes due to increased structural disorder and localized strain [46].

Thus, it may be inferred from the Raman and PL analysis of ZnO films that the observed defects in ZnO films are primarily due to Zn interstitials and oxygen vacancies. To validate this, we have utilized DFT investigations.

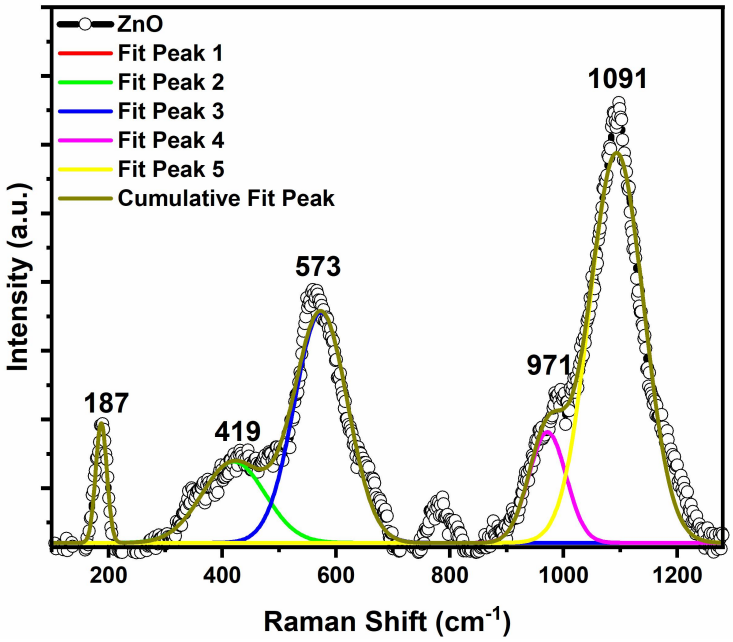

Figure 9. Deconvoluted Raman spectra of ZnO thin film.

3.5 Validation of experiment: A first-principles based on DFT study

We conducted a first-principles DFT study of the ZnO structure to validate the experimental finding. Details regarding the computational methodology are provided in the Materials and Methods section. The geometrical structure of ZnO was optimized to refine its structure and to study its electronic band structure and optical properties.

3.5.1 Structural properties

Before and after the geometry optimization, the lattice parameter of ZnO was extracted from the simulation studies, as indicated in Table 1. The result obtained is in agreement with the results of Ma *et al*.[47] Results and the experimental study (JCPDS file = 00-036-1451); however, a slight deviation in the lattice parameter was observed, which might be due to the structure refinement.

Table 1. Structural properties of ZnO obtained before and after the geometrical optimization.

Structures	Lattice parameters	GGA-PBE calculated results	JCPDS #00-36-1451
Before geometry optimization ZnO	a (Å) =b (Å)	3.22	3.25
	c (Å)	5.20	5.20
	Cell volume (Å^3)	46.69	47.62
	Cell angle (°)	α=90°, β=90°, γ=120°	α=90°, β=90°, γ=120°
Optimized ZnO structure	a (Å)=b (Å)	3.35	-
	c (Å)	5.24	-
	Cell volume(Å^3)	51.112	-
	Cell angle (°)	α=90°, β=90°, γ=120°	-

3.5.2 Total Density of State (DOS)

Figure 10 depicts ZnO's total density of states (TDOS) at energy levels ranging from -30 eV valence band to 30 eV conduction band, with a Fermi level set at zero. The data analysis results indicate that the PDOS of Zn was mainly contributed by Zn 3d and Zn 4s orbital states. In comparison, O atoms were contributed by the O 2p and O 2s orbital states. The graph shows that the valence band is mainly composed of Zn 3d and O 2s orbitals at the topmost level, while O 2p orbitals are at a lower level near the Fermi level. Meanwhile, the conduction band is mainly composed of Zn 4s and O 2p orbitals at the bottom. Therefore, O 2p at the topmost of the valence band and Zn 4s orbital state at the bottom of the conduction band are mainly responsible for getting a realistic band structure of ZnO. A similar analysis was reported using DFT in published articles [24]43].

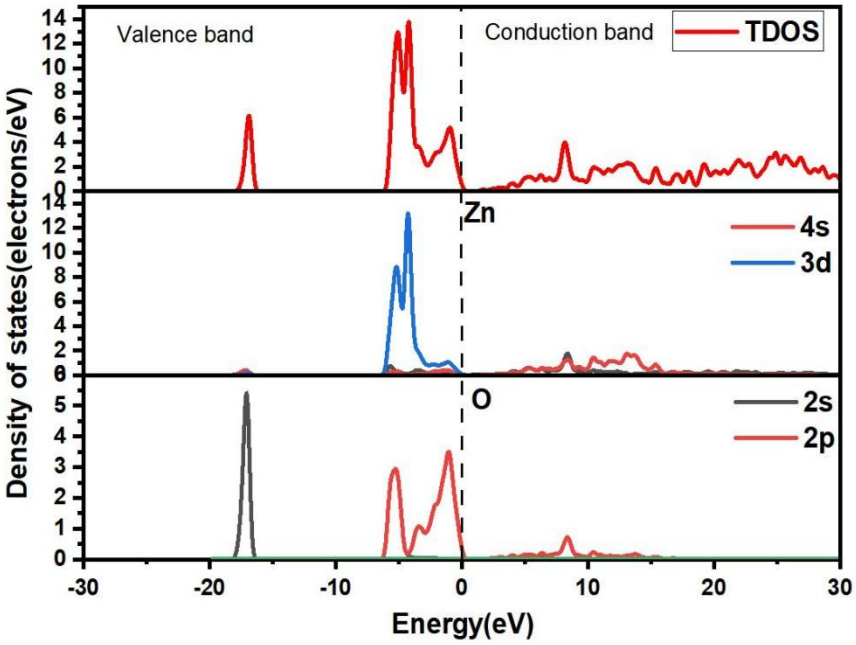

Figure 10. Density of states (DOS) of ZnO.

3.5.3 Electronic band structure

The electronic band structure of ZnO was calculated using a GGA-based study and found to be 3.37 eV, similar to that reported by Jafarova *et al*. [49] and Harun *et al*. [50] shown in Figure 12A, which was observed to be much lower than the experimentally realized result of the experimental energy band gap (E_g), because DFT is based on ground-state theory and severely underestimates the exchange-correlation potential between excited electronic states [30]. Therefore, an LDA+U-based study evolved to correct the electronic band structure. The Hubbard U parameter $U_{d\text{-}Zn}$(8.7) and $U_{p\text{-}O}$ (7.2)[51], resulting in an energy bandgap(~3.37 eV), as experimental findings with little variation. This small gap between the experimental and theoretical value indicates close to ideal behaviour. The small deviation likely arises due to the microstructural effects of grain size and crystallinity.The theoretical energy bandgap corrected was consistent with the published report [24][22][47] as shown in Figure 11B. The results indicate ZnO as a direct bandgap semiconductor, *i.e*., the valence band's topmost energy level and the conduction band's bottom energy level meeting at the same point (G-G point)[24].

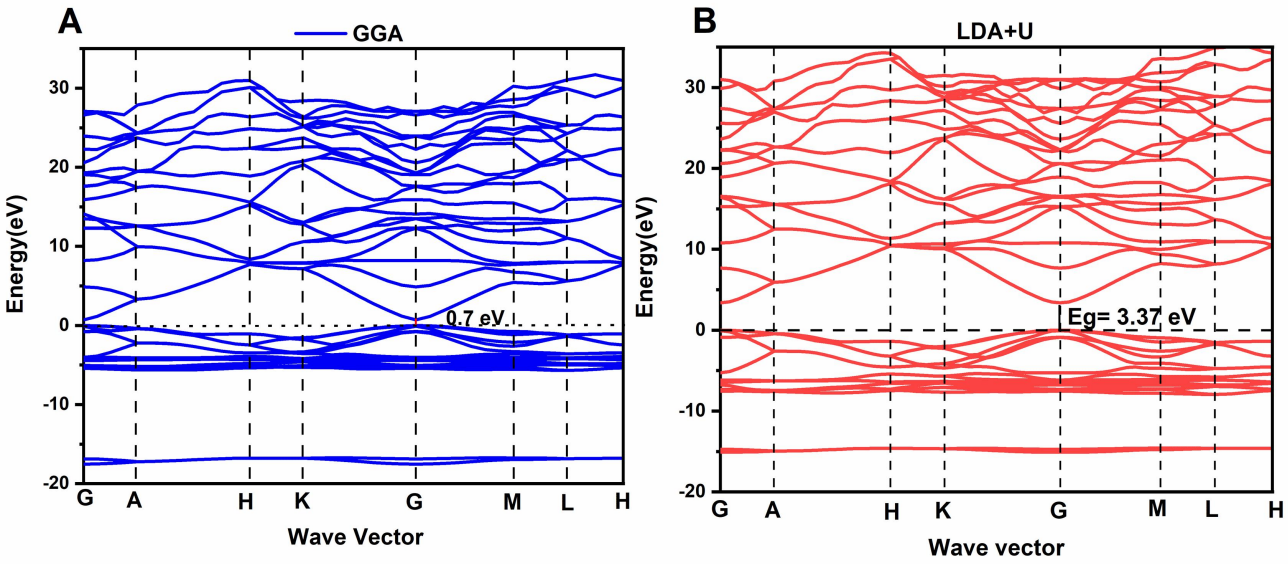

Figure 11. Electronic band structure of ZnO obtained after (A) GGA study & (B) LDA+U study.

3.5.4 Optical properties

3.5.4.1 Dielectric constant

Optical properties of any material are attributed to the complex dielectric function formula, which may be represented as follows in equation (4) [52].

$$\varepsilon(\omega) = \varepsilon_1(\omega) + i\varepsilon_{2(}\omega) \qquad (4)$$

Where ε_1 and ε_2 are the dielectric function's real and imaginary components. The optical characteristics (absorption coefficient, reflectance, and loss of function) are described by the imaginary part (ε_2), while the real part (ε_1) indicates the amount of energy stored in the material [53][54][55]. Here, we will discuss the imaginary part (ε2) of the optical properties. ε_2 can be generated by incorporating the transition between the occupied and unoccupied electronic states, as succinctly discussed in our prior report [55]. Figures 12(A) and (B) show the plot of both the real part (ε_1) and imaginary (ε_2) part of ZnO obtained after DFT calculations, which are plotted in a wide range of 0-50 eV energy levels. Figure 12(B) depicts the dielectric function's imaginary (ε_2) part, revealing three prominent peaks at 2.14 eV, 6.46 eV, and 10.1 eV, respectively. The primary intense peak (10.1 eV) might be attributed to band-to-band transitions of electrons from the upper O-2p valence band to the lower Zn-4s conduction band states, as stated in the density of states section. Further, other optical properties such as absorption coefficient, reflectivity, and dielectric loss, which are related to the imaginary part of the dielectric function, are briefly explained.

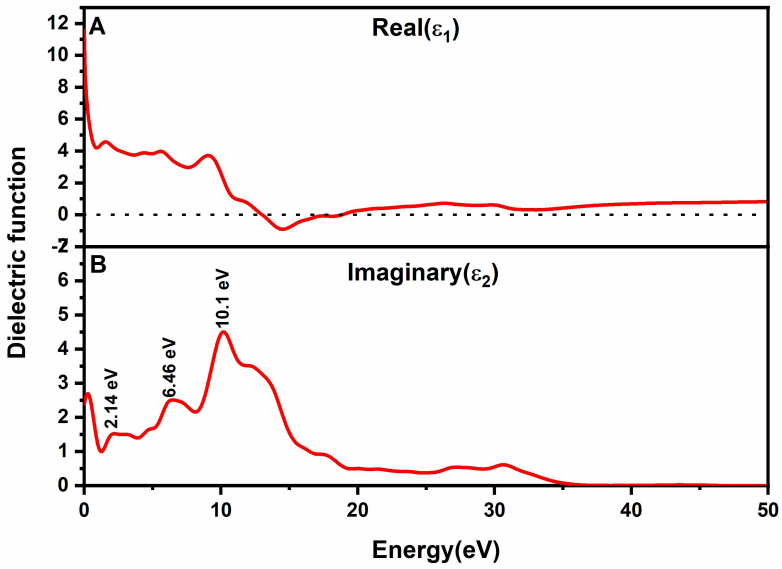

Figure 12. Dielectric constant vs Energy(eV) graph of ZnO.

Figure 13A depicts ZnO's absorption vs. wavelength (nm) graph derived from the DFT investigation. After analysing the graph, the absorption edge was observed at ~393 nm, consistent with our experimental findings (393 nm). Furthermore, we investigated other optical properties, *i.e.*, ZnO's reflectivity and loss of function. Figure 13B depicts the reflectivity vs energy(eV) graph in the 0-50 eV energy level range, where reflectivity is attributed to the material's capability to reflect the incident light from its surface. The graph's analysis shows that the maximum reflectivity is 0.33 at an energy level of 14.67. When achieving the highest reflectivity (0.33), a decrease in reflectance might be due to an electron excitation into higher-energy states or to increased photon penetration depth into the material. This type of behaviour attributes suitable potential for optoelectronic devices and solar cells. Moreover, loss-of-function was also studied. Figure 13C depicts the loss of function vs energy (eV) graph, which describes where and how much energy a fast electron loses because of interactions with the material's electronic structure while passing through it. Peaks (19.31 eV and 32.8 eV) in the loss function vs energy (eV) graph indicate energies where the fast electron loses energy effectively.

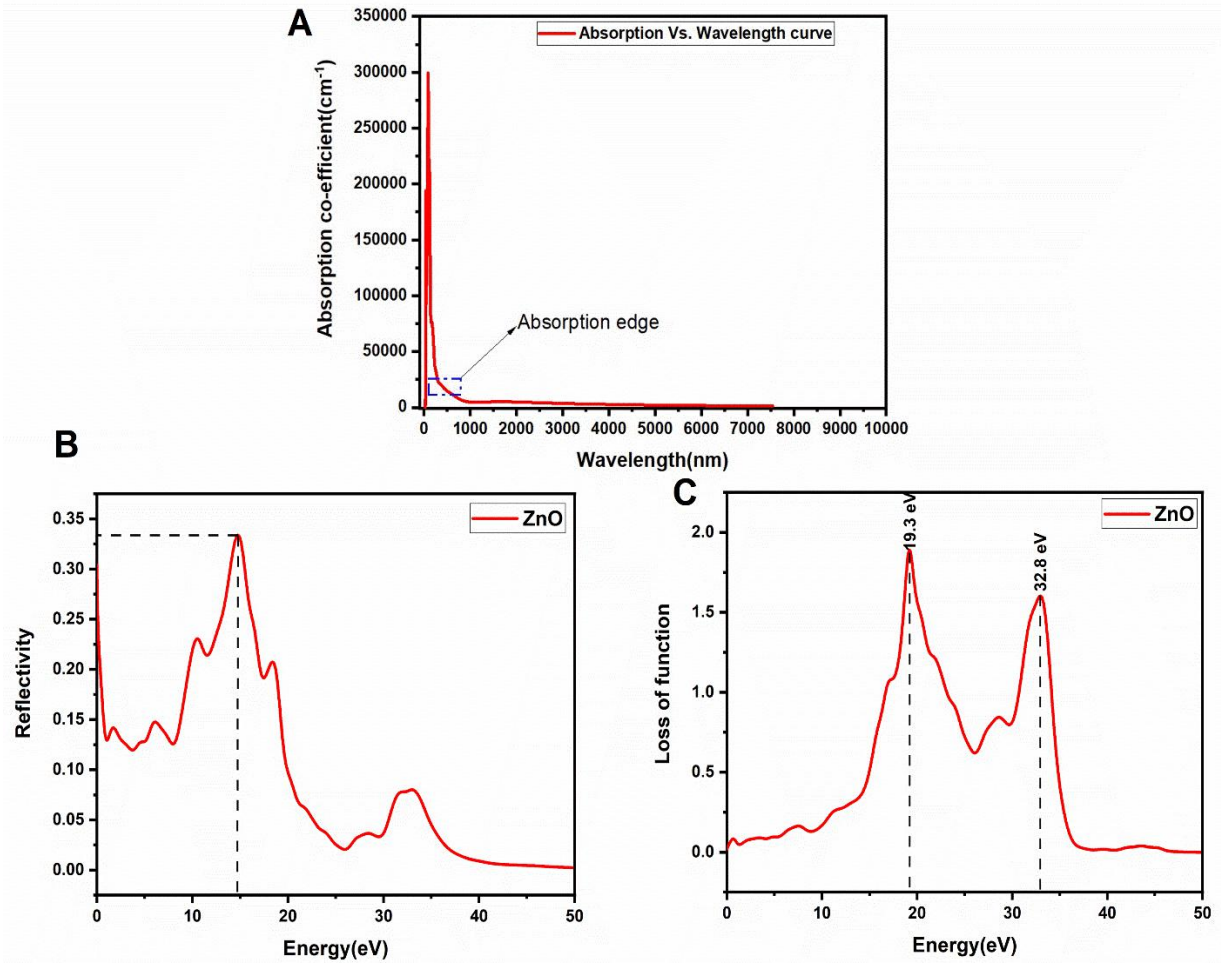

Figure 13. (A) plot of absorption coefficient vs. wavelength, (B) Reflectivity vs. Energy(eV), and (C) loss of function vs. Energy(eV) of ZnO.

3.5.5 Raman analysis

Furthermore, to validate our experimental Raman results with a theoretical study, we performed a computational analysis of the Raman spectra of the wurtzite ZnO structure. The simulated Raman data, shown in Figure 14, reveal two prominent peaks at approximately 334 cm^{-1} and 433 cm^{-1}, which closely agree with our experimental findings. The peak at 334 cm^{-1} is attributed to a second-order Raman process, precisely a combination of the E2(high) and E2 (low) phonon modes, consistent with wurtzite ZnO [41]. The peak at 433 cm^{-1} corresponds to the E2(high) mode, a characteristic first-order Raman-active vibration associated with the oxygen atoms in the ZnO lattice. The defect level obtained from the theoretical Raman spectra differs slightly from that in the experimental Raman spectra, indicating that defects in ZnO films arise during film formation, nucleation, and growth, or from impurities. Thus, the obtained results confirm the presence of the wurtzite phase ZnO and support our experimental Raman data.

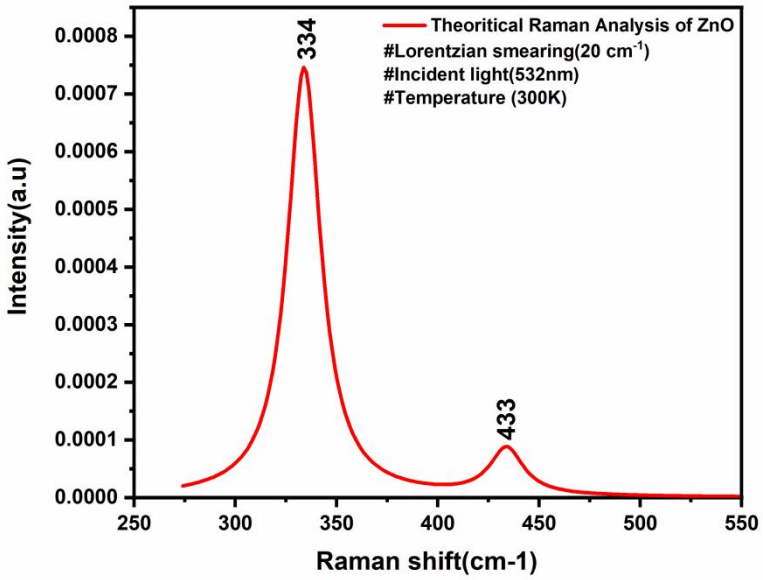

Figure 14. Computational study-based Raman spectra of ZnO thin film.

4. Discussion

ZnO thin film using the sol-gel method was successfully deposited on pre-patterned fluorine-doped tin oxide-coated glass (FTO) substrates. Further, various characterization methods, such as SEM, EDX, XRD, AFM, UV-Visible spectroscopy, PL spectroscopy, and Raman analysis, have evolved to study the morphological, structural, and optical properties of the grown thin films. Upon analysis of the SEM micrograph, it was observed that the thin film was uniformly distributed over the substrate, with no defects. Furthermore, XRD results indicate that the thin films exhibit a polycrystalline structure with an average crystallite size of 16.21 ± 0.5 nm. The optical absorption edge of the thin film was observed at 393 nm, with an energy bandgap of 3.39 eV. In the PL analysis, PL spectra of ZnO films with peaks at 375 nm (NBE) and at 502, 567, 592, and 745 nm (DLE) were observed. These DLE emissions are linked to oxygen vacancies, interstitials, and zinc interstitials. The 745 nm NIR peak is due to deep-level transitions. Defect emissions can be tuned by doping, annealing, or surface passivation. In the Raman analysis, the ZnO thin film shows peaks at 187 cm^{-1}, 419 cm^{-1}, 573 cm^{-1}, 777 cm^{-1}, 971 cm^{-1}, and 1091 cm^{-1}. The bands at 417 cm^{-1} and 573 cm^{-1} correspond to E2 (high) and A1 (LO) modes of the ZnO wurtzite structure, while those at 187 cm^{-1}, 971 cm^{-1}, and 1091 cm^{-1} are attributed to second-order LO combinations and overtones. The 187 cm^{-1} peak also indicates Zn interstitial defects, and the asymmetric peaks at 419 cm^{-1} and 573 cm^{-1} are linked to oxygen vacancies. These observations suggest that Zn interstitials and oxygen vacancies dominate the defect structure. Further, to support the experimental finding, a first-principles DFT study was conducted to validate it. The structural properties obtained in the DFT study were consistent with experimental data for ZnO. Also, the electronic band structure (3.37 eV) and absorption edge (393 nm) obtained from the DFT calculation agreed with the experimental findings. Raman analysis indicates the same for wurtzite ZnO. The above results suggest that ZnO thin films deposited by the spin-coating-based sol-gel method may be suitable for optoelectronic and solar cell applications.

.

5. Conclusions

In the present study, we comprehensively investigated the structural, optical, and Raman properties of sol-gel-synthesized ZnO thin films using a combination of experimental and theoretical approaches. SEM, AFM, XRD, and UV-Vis. Analysis revealed that the ZnO films exhibit a uniform surface morphology with an average surface roughness of 5.5 ± 0.5 nm and a wurtzite crystal structure with an optical bandgap of 3.39 eV. Furthermore, PL and Raman analyses were performed to investigate defects within the ZnO thin film. The PL analysis reveals that the thin film consists of various non-radiative deep-level emission defects at 502 nm, 567 nm, and 592 nm, corresponding to green, yellow-green, and yellow emission bands, respectively. Raman analysis also suggests the presence of defect levels arising from oxygen interstitials and oxygen vacancies. These experimental findings were further validated using DFT investigations. The structural and optical properties obtained in the DFT study were consistent with the experimental findings for the sol-gel-synthesized ZnO thin film. Also, the electronic band structure (3.37 eV) and absorption edge (393 nm) obtained from the DFT calculation agreed with the experimental findings. DOS analysis of ZnO indicates that O 2p at the topmost of the valence band and Zn 4s orbital state at the bottom of the conduction band are mainly responsible for getting a realistic band structure. Moreover, the defect level obtained from the theoretical Raman spectra differs slightly from that in the experimental Raman spectra, indicating that the defects in ZnO films arise during formation, nucleation, and growth, or from impurities. Thus, the present work synergistically explains and validates the structural and optical properties of ZnO films. Such results are necessary to correlate with the experimental and theoretical results of wide-bandgap materials, which are crucial for solar cell applications.

Abbreviations

ZnO, Zinc oxide; DFT, Density functional theory; DOS, density of states; PL,photoluminescence

Availability of data and materials: The data supporting this study's findings are available from the corresponding author upon request.

Author contributions:

Pramod Mandal: Contributed toward formal analysis, data curation, methodology, investigation, writing-original draft, conceptualization, and visualization.

Anand Pandey: Contributed toward visualization, conceptualization, discussion, writing, review, and editing.

Sudesna Roy: Contributed toward formal analysis, validation, Supervision, administration, and writing-review and editing.

Acknowledgment: The authors sincerely thank the Department of Graphic Arts and Photophysics, Faculty of Chemical Technology, University of Pardubice, Czech Republic, for their kind support with DFT software and the English-language editing tool, which improved the manuscript's language.

Conflict of Interest: The authors declare that they have no known competing financial interests or personal relationships that could have appeared to influence the work reported in this paper.

Declaration of AI and AI-assisted Technologies in the Writing Process:

We declare that we used English-language editing software, such as Grammarly, to improve the manuscript's language.

References

1. Alasmari, A.; Awad, A.A.; Aboud, A.A. Investigating the influence of yttrium doping on physical properties of ZnO thin films deposited via spray pyrolysis. *Optical Materials (Amsterdam)* 2024, 148, 114899. https://doi.org/10.1016/j.optmat.2024.114899
2. Ozel, K. Strain-induced photoresponsivity in gallium-doped ZnO thin film based UV photodetectors. *Sensors and Actuators A: Physical* 2024, 366, 114953. https://doi.org/10.1016/j.sna.2023.114953
3. Benrezgua, E.; Deghfel, B.; Zoukel, A.; Basirun, W.J.; Amari, R.; Boukhari, A.; Yaakob, M.K.; Kheawhom, S.; Mohamad, A.A. Synthesis and properties of copper doped zinc oxide thin films by sol-gel, spin coating and dipping: A characterization review. *Journal of Molecular Structure* 2022, 1267, 133639. https://doi.org/10.1016/j.molstruc.2022.133639
4. Jain, S.; Medlin, W.; Uprety, S.; Isaacs-Smith, T.; Olsson, T.; Davis, J.; Burrows, S.; Chumley, S.; Park, M.; Laurent, G.M. Nanosecond-laser annealing of zinc oxide thin-films: The effect of the laser wavelength and fluence. *Thin Solid Films* 2024, 791, 140236. https://doi.org/10.1016/j.tsf.2024.140236
5. Buzok, E.B.; Yalcin, S.; Demircan, G.; Yılmaz, D.; Aktas, B.; Aytar, E. The structural, optical, electrical and radiation shielding properties of Co-doped ZnO thin films. *Radiation Physics and Chemistry* 2024, 222, 111840. https://doi.org/10.1016/j.radphyschem.2024.111840
6. Davis, K.; Yarbrough, R.; Froeschle, M.; White, J.; Rathnayake, H. Band gap engineered zinc oxide nanostructures: Via a sol-gel synthesis of solvent driven shape-controlled crystal growth. *RSC Advances* 2019, 9(26), 14638–14648. https://doi.org/10.1039/c9ra02091h
7. Amakali, T.; Daniel, L.S.; Uahengo, V.; Dzade, N.Y.; de Leeuw, N.H. Structural and Optical Properties of ZnO Thin Films Prepared by Molecular Precursor and Sol–Gel Methods. *Crystals* 2020, 10(2), 132. https://doi.org/10.3390/cryst10020132
8. Mousavi, S.S.; Sajad, B.; Majlesara, M.H. Fast response ZnO/PVA nanocomposite-based photodiodes modified by graphene quantum dots. *Materials & Design* 2019, 162, 249–255. https://doi.org/10.1016/j.matdes.2018.11.037
9. Haddad, O.; Ait hssi, A.; Soussi, A.; Labchir, N.; Smiri, B.; Abouabassi, K.; Markazi, R.; Elfanaoui, A.; Ihlal, A. Structural, optical, and morphological properties of electrochemically synthesized Bi-doped ZnO nanorods for photovoltaic applications: Insights from DFT calculations. *Optical Materials (Amsterdam)* 2025, 160, 116763. https://doi.org/10.1016/j.optmat.2025.116763
10. Kumar, M.; Dhar, J.C. Defect engineering of RF sputtered Mg doped ZnO thin film for efficient photodetector application. *Micro and Nanostructures* 2024, 185, 207724. https://doi.org/10.1016/j.micrna.2023.207724
11. Kermiche, F.; Taabouche, A.; Bouabellou, A.; Hanini, F.; Bouachiba, Y. Behavior Study of ZnO Thin Films Grown by PLD for Several Applications. *Crystallography Reports* 2022, 67, 1239–1245. https://doi.org/10.1134/S1063774522070069
12. Fasquelle, D.; Députier, S.; Bouquet, V.; Guilloux-Viry, M. Effect of the Microstructure of ZnO Thin Films Prepared by PLD on Their Performance as Toxic Gas Sensors. *Chemosensors* 2022, 10(7), 285. https://doi.org/10.3390/chemosensors10070285
13. Li, Q.; Ying, M.; Zhang, M.; Cheng, W.; Li, W.; Liao, B.; Zhang, X. Structural characterization and surface polarity determination of polar ZnO films prepared by MBE. *Applied Nanoscience* 2023, 13, 3197–3204. https://doi.org/10.1007/s13204-021-01978-2
14. Mezher, S.J.; Kadhim, B.B.; Dawood, M.O. Synthesis and characterization of Au–ZnO nanorods growth by CVD method. *Optical and Quantum Electronics* 2023, 55, 1–15. https://doi.org/10.1007/s11082-023-05072-5
15. MohammadZaheri, M.; Esfahani, H. The effects of nanofibrous seed layer and stoichiometry of CBD process on microstructural, electro-optical and photocatalytic activity of ZnO nanorods for oxytetracycline degradation. *Journal of Photochemistry and Photobiology A: Chemistry* 2023, 438, 114564. https://doi.org/10.1016/j.jphotochem.2023.114564

16. Mishra, M.; Banga, V.P.; Kumar, M.; Gupta, M. Effect of aging on transmittance, and effect of annealing temperature on CO2 sensing of ZnO thin film deposited by spin coating. *e-Prime - Advances in Electrical Engineering, Electronics and Energy* 2024, 7(10), 100405. https://doi.org/10.1016/j.prime.2023.100405
17. Shafi, M.A.; Bouich, A.; Fradi, K.; Guaita, J.M.; Khan, L.; Mari, B. Effect of deposition cycles on the properties of ZnO thin films deposited by spin coating method for CZTS-based solar cells. *Optik (Stuttgart)* 2022, 258, 168854. https://doi.org/10.1016/j.ijleo.2022.168854
18. Bouderbala, I.Y.; Guessoum, A.; Rabhi, S.; Bouhlassa, O.; Bouras, I.E. Optical band-diagram, Urbach energy tails associated with photoluminescence emission in defected ZnO thin films deposited by sol–gel process dip-coating: effect of precursor concentration. *Applied Physics A: Materials Science & Processing* 2024, 130(3), 205. https://doi.org/10.1007/s00339-024-07366-1
19. Ben Moussa, N.; Lajnef, M.; Jebari, N.; Villebasse, C.; Bayle, F.; Chaste, J.; Madouri, A.; Chtouroub, R.; Herth, E. Synthesis of ZnO sol-gel thin-films CMOS-Compatible. *RSC Advances* 2021, 11(37), 22723–22733. https://doi.org/10.1039/D1RA02241E
20. Rojano Chávez, S.M.; Ayala, L.M.; Karthik, T.V.K.; Maldonado, A.; Gómez-Pozos, H. Zinc oxide thin films deposited by sol–gel spin-coating technique for propane and carbon monoxide sensing applications. *Journal of Materials Science: Materials in Electronics* 2024, 35, 797. https://doi.org/10.1007/s10854-024-12502-x
21. Fedorenko, A.V.; Bozhko, K.M.; Kachur, N.V.; Kosiakovskiy, A.V.; Maslov, V.P. Optical and electrical properties of zinc oxide nanofilms deposited using the sol-gel method. *Semiconductor Physics, Quantum Electronics & Optoelectronics* 2024, 27(1), 117–123. https://doi.org/10.15407/spqeo27.01.117
22. Wang, J.; Shen, T.; Feng, Y.; Liu, H. A GGA+U study of electronic structure and the optical properties of different concentrations Tb doped ZnO. Physica B: Condensed Matter 2020, 576, 411720. https://doi.org/10.1016/j.physb.2019.411720
23. Yaakob, M.K.; Hussin, N.H.; Taib, M.F.M.; Kudin, T.I.T.; Hassan, O.H.; Ali, A.M.M.; Yahya, M.Z.A. First principles LDA+U calculations for ZnO materials. *Integrated Ferroelectrics* 2014, 155(1), 15–22. https://doi.org/10.1080/10584587.2014.905086
24. S. Mansy, H. Musleh, S. Shaat, J. Asad, and N. AlDahoudi, "Computational and experimental study of wurtzite phase ZnO nanoparticles," *Mater. Today Commun.*, vol. 35, no. December 2022, p. 105688, 2023, doi: 10.1016/j.mtcomm.2023.105688.
25. Pandey, A.; Garg, A.; Kumar, L. Microstructural, Optical, and Work Function Tuning of Fullerene (C60) Modified Zinc Oxide Films for Optoelectronic Devices. *ECS Journal of Solid State Science and Technology* 2022, 11, 104002. https://doi.org/10.1149/2162-8777/ac949f
26. Mandal, P.; Roy, S. Ultra-Wide Bandgap ß-gallium Oxide (Ga_2O_3) Advancing Next-Generation Defense Technologies. In *Innovative Materials for Next-Generation Defense Applications: Cost, Performance, and Mass Production*; Güler, O.; Çelebi, M.; Karabacak, A., Eds.; IGI Global Scientific Publishing, 2025; pp. 353–398. https://doi.org/10.4018/979-8-3373-0933-0.ch011
27. Segall, M.D.; Lindan, P.J.D.; Probert, M.J.; Pickard, C.J.; Hasnip, P.J.; Clark, S.J.; Payne, M.C. First-principles simulation: Ideas, illustrations and the CASTEP code. *Journal of Physics: Condensed Matter* 2002, 14(11), 2717–2744. https://doi.org/10.1088/0953-8984/14/11/301
28. Clark, S.J.; Segall, M.D.; Pickard, C.J.; Hasnip, P.J.; Probert, M.I.J.; Refson, K.; Payne, M.C. First principles methods using CASTEP. *Zeitschrift für Kristallographie* 2005, 220(5-6), 567–570. https://doi.org/10.1524/zkri.220.5.567.65075
29. Mandal, P.; Singh, U.P.; Roy, S. Structure-property correlation of europium doped β-Ga2O3: an experimental and first-principle study. *Journal of Materials Science: Materials in Electronics* 2023, 34, 1–16. https://doi.org/10.1007/s10854-023-11455-x
30. Mandal, P.; Mondal, A.; Pandey, A.; Romeo, S.; Bag, A. Investigating role of annealing in shaping morphological, structural, tribological, and optical characteristics of gallium oxide (Ga2O3): Insights from DFT analysis. *Journal of Alloys and Compounds* 2025, 1011, 178367. https://doi.org/10.1016/j.jallcom.2024.178367

31. Hadi, A.J.; Nayef, U.M.; Mutlak, F.A.H.; Jabir, M.S. High-Efficiency Photodetectors Based on Zinc Oxide Nanostructures on Porous Silicon Grown by Pulsed Laser Deposition. *Plasmonics* 2024, 19(2), 577–593. https://doi.org/10.1007/s11468-023-02016-3
32. Alibeigi, A.N.; Javid, N.; Amiri Gharaghani, M.; Honarmandrad, Z.; Parsaie, F. Synthesis, characteristics, and photocatalytic activity of zinc oxide nanoparticles stabilized on the stone surface for degradation of metronidazole from aqueous solution. *Environmental Health Engineering and Management* 2021, 8(1), 55–63. https://pdfs.semanticscholar.org/5fcc/e3dce8d005faf71f02b2d397931a9c58d3bd.pdf
33. Lee, P.; Chang, S.; Chang, J.; Hsu, E.; Chang, S. Highly Transparent Nanostructured Zinc Oxide Photodetector Prepared by Successive Ionic Layer Adsorption and Reaction. *International Journal of Electrochemical Science* 2013, 8(5), 6425–6432. https://doi.org/10.1016/S1452-3981(23)14773-0
34. Elilarassi, R.; Chandrasekaran, G. Effect of annealing on structural and optical properties of zinc oxide films. *Materials Chemistry and Physics* 2010, 121(1-2), 378–384. https://doi.org/10.1016/j.matchemphys.2010.01.053
35. Pandey, A.; Tyagi, S.; Singh, B.P.; Kumar, L. Surface morphological and optical evolution of RF sputtered AZO films for optoelectronic devices. *Physica B: Condensed Matter* 2022, 647(6), 414393. https://doi.org/10.1016/j.physb.2022.414393
36. Kabir, A.; Bouanane, I.; Boulainine, D.; Zerkout, S.; Schmerber, G.; Boudjema, B. Photoluminescence Study of Deep Level Defects in ZnO Thin Films. *Silicon* 2019, 11(2), 837–842. https://doi.org/10.1007/s12633-018-9876-2
37. Sahu, J.; Kumar, S.; Vats, V.S.; Alvi, P.A.; Dalela, B.; Kumar, S.; Phase, D.M.; Gupta, M.; Dalela, S. Exploring the Defects and Vacancies with Photoluminescence and XANES Studies of Gd3+-Substituted ZnO Nanoparticles. *Particle & Particle Systems Characterization* 2022, 39(10), 1–19. https://doi.org/10.1002/ppsc.202200116
38. Crapanzano, R.; Villa, I.; Mostoni, S.; D'Arienzo, M.; Di Credico, B.; Fasoli, M.; Scotti, R.; Vedda, A. Morphology related defectiveness in zno luminescence: From bulk to nano-size. *Nanomaterials* 2020, 10(10), 1983. https://doi.org/10.3390/nano10101983
39. Akazawa, H. Identification of defect species in ZnO thin films through process modification and monitoring of photoluminescent properties. *Journal of Vacuum Science & Technology A: Vacuum, Surfaces, and Films* 2019, 37(6), 061514. https://doi.org/10.1116/1.5121439
40. Lima, L.; de S. Caldas, L.; Alí, A.; Barreto, J.; Freitas, R.; Mazzarella, A.; Felix, G.; Carozo, V.; Stavale, F. Growth and Raman spectroscopy of ultrathin ZnO(0001) films on Ag(001). *Surface Science* 2021, 704, 121748. https://doi.org/10.1016/j.susc.2020.121748
41. Koyano, M.; QuocBao, P.; ThanhBinh, L.T.; HongHa, L.; NgocLong, N.; Katayama, S. Photoluminescence and Raman spectra of ZnO thin films by charged liquid cluster beam technique. *Physica Status Solidi A: Applied Research* 2002, 193(1), 125–131. https://doi.org/10.1002/1521-396X(200209)193:1<125::AID-PSSA125>3.0.CO;2-X
42. Sharma, A.; Singh, B.P.; Dhar, S.; Gondorf, A.; Spasova, M. Effect of surface groups on the luminescence property of ZnO nanoparticles synthesized by sol-gel route. *Surface Science* 2012, 606(3-4), L13-L17. https://doi.org/10.1016/j.susc.2011.09.006
43. Song, Y.; Zhang, S.; Zhang, C.; Yang, Y.; Lv, K. Raman spectra and microstructure of zinc oxide irradiated with swift heavy ion. *Crystals* 2019, 9(8), 395. https://doi.org/10.3390/cryst9080395
44. de S. e. Silva, R.L.; Franco, A. Raman spectroscopy study of structural disorder degree of ZnO ceramics. *Materials Science in Semiconductor Processing* 2020, 119(3), 105227. https://doi.org/10.1016/j.mssp.2020.105227
45. Le Guellec, M.; Lebreton, F.; Ramond, L.; Martin, P.; Ndiaye, A.; Gervais, T.; Bernard-Granger, G. Grain size analysis and characterization by Raman spectroscopy of a homogeneous sintered MOX fuel. *Journal of the European Ceramic Society* 2022, 42(16), 7553–7560. https://doi.org/10.1016/j.jeurceramsoc.2022.09.017
46. Keshav, R.; MG, M. Photoluminescence and Raman spectroscopic analysis of PV deposited ZnS thin films. *Materials Research Bulletin* 2018, 105, 360–367. https://doi.org/10.1016/j.materresbull.2018.05.018

47. Ma, X.; Wu, Y.; Lv, Y.; Zhu, Y. Correlation effects on lattice relaxation and electronic structure of zno within the GGA+U formalism. *The Journal of Physical Chemistry C* 2013, 117(49), 26029–26039. https://doi.org/10.1021/jp407281x
48. Mohamad, A.A.; Hassan, M.S.; Yaakob, M.K.; Taib, M.F.M.; Badrudin, F.W.; Hassan, O.H.; Yahya, M.Z.A. First-principles calculation on electronic properties of zinc oxide by zinc–air system. *Journal of King Saud University - Engineering Sciences* 2017, 29(3), 278–283. https://doi.org/10.1016/j.jksues.2015.08.002
49. Jafarova, V.N.; Orudzhev, G.S. Structural and electronic properties of ZnO: A first-principles density-functional theory study within LDA(GGA) and LDA(GGA)+U methods. *Solid State Communications* 2021, 325, 114166. https://doi.org/10.1016/j.ssc.2020.114166
50. Harun, K.; Salleh, N.A.; Deghfel, B.; Yaakob, M.K.; Mohamad, A.A. DFT + U calculations for electronic, structural, and optical properties of ZnO wurtzite structure: A review. *Results in Physics* 2020, 16(9), 102829. https://doi.org/10.1016/j.rinp.2019.102829
51. Merdan, M.; Banimuslem, H.A. Synthesis, characterization and LDA+U calculations of zinc oxide nanoparticles. *Physica Scripta* 2024, 99(6), 065942. https://doi.org/10.1088/1402-4896/ad4427
52. Ma, X.; Zhang, Y.; Dong, L.; Jia, R. First-principles calculations of electronic and optical properties of aluminum-doped β-Ga2O3 with intrinsic defects. *Results in Physics* 2017, 7, 1582–1589. https://doi.org/10.1016/j.rinp.2017.04.023
53. Ping, L.K.; Mohamed, M.A.; Mondal, A.K.; Taib, M.F.M.; Samat, M.H.; Berhanuddin, D.D.; Menon, P.S.; Bahru, R. First-principles studies for electronic structure and optical properties of strontium doped β-ga2o3. *Micromachines* 2021, 12(4), 348. https://doi.org/10.3390/mi12040348
54. Dang, J.N.; Zheng, S.W.; Chen, L.; Zheng, T. Electronic structures and optical properties of Si- and Sn-doped β-Ga2O3: A GGA+U study. *Chinese Physics B* 2019, 28(1), 016301. https://doi.org/10.1088/1674-1056/28/1/016301
55. Mandal, P.; Kumar, S.; Pandey, A.; Katariya, L.; Mondal, A.; Bag, A. Unveiling structural and optical properties of Sn-doped β-Ga2O3: A correlation of experimental and theoretical observations. *Materials Science and Engineering: B* 2024, 302(12), 117266. https://doi.org/10.1016/j.mseb.2024.117266

© 2026 by the authors. Submitted for possible open access publication under the terms and conditions of the Creative Commons Attribution (CC BY) license (http://creativecommons.org/licenses/by/4.0/).